A Postprocessing-Technique-Based Switching Loss Estimation Method for GaN Devices

Minghai Dong, *Student Member, IEEE*, Hui Li, *Senior Member, IEEE*, Shan Yin, *Member, IEEE*, Yingzhe Wu, *Member, IEEE*, and Kye Yak See, *Senior Member, IEEE*

***Abstract*—Gallium nitride (GaN) high electron mobility transistor (HEMT) is a promising candidate for the high-density power converter applications. Due to the low switching loss, the GaN HEMT may lead to a new horizon in the applications, such as fast charger, wireless charging, and 5G power amplifier. However, the fast switching speed of GaN HEMT makes it extremely sensitive to parasitic parameters, especially for the low-voltage GaN devices with small packages. Conventional switching loss estimation methods, which are normally based on the calibration fixture or modification of test circuit, cannot be effectively utilized for GaN HEMT. This article presents an accurate switching loss estimation method using the postprocessing technique. The proposed switching loss technique consists of three parts of signal processing, which are the wavelet denoising process to minimize the influence of background noise, the voltage–current ($V-I$) alignment process to reduce errors from probe propagation delay, and the linear interpolation process for further improvement of alignment accuracy. In addition, a modified SPICE model is proposed to investigate the influence of parasitic parameters on switching losses by the circuit simulation. Based on the theoretical switching characteristics, the switching loss estimation method is finally validated experimentally on a commercial 40-V/10-A GaN HEMT in a double-pulse test.**

***Index Terms*—Double-pulse test, gallium nitride (GaN), signal processing, switching characterization, switching loss estimation.**

I. Introduction

GALLIUM nitride (GaN) high electron mobility transistor (HEMT) is a promising candidate for the high-density power converter applications, such as fast charger, wireless charging, and 5G power amplifier [1]–[3]. Due to the advantages of wide bandgap (WBG) material, it has lower ON-resistance, lower parasitic capacitance, higher junction temperature, and higher switching speed compared with traditional silicon (Si) devices. As a lateral device, the GaN HEMT is fabricated on AlGaN/GaN heterojunction interface, which generates the two-dimensional electron gas (2DEG). It eliminates the p-n junction and leads to the zero reverse recovery charge ($Q_{\rm rr}$). Thus, it allows the GaN HEMT to operate in the MHz-frequency power converter with a high energy conversion efficiency [4]–[7]. When the switching frequency enters the MHz range, the switching loss of GaN HEMT becomes significant.

However, most of the device datasheets only provide limited information on the switching loss. Furthermore, the loss is strongly dependent on the circuit parameters. As a consequence, the switching loss characterization becomes crucial for the GaN-based converter design. So far, early works on the switching loss characteristics of GaN HEMT can be mainly classified into model-based [8]–[13] and measurement-based approaches [14]–[18].

The model-based approach requires accurate derivation of the behavioral or analytical models [9], [10], which can be a time-consuming and cumbersome process. Therefore, the measurement-based approach is usually preferred. This approach adopts two methods, the calorimetric and the double-pulse test (DPT) methods. The calorimetric method uses a calorimeter (such as an air flow meter [14]) to obtain the switching loss through capturing the temperature change, but it is challenging to obtain the breakdown of various loss mechanisms [18]. The DPT method acquires the time-domain voltage and current switching waveforms and performs the integration over time. Although there are drawbacks of DPT [19], such as the requirements of high-precision probes and an exact voltage–current ($V-I$) alignment method, it is still considered as the most feasible method with reasonable accuracy [20]. By applying postprocessing technique, the influences from the probes and voltage–current misalignment can be minimized to improve the accuracy [21], [22].

Conventionally, probe manufacturers provide dedicated calibration fixtures for measuring instruments but only compatible with selected probes [23]. For example, the compensation output of an oscilloscope was used as the reference signal but it is only compatible to a limited selection of voltage or current probes [24]. Alignment of $V-I$ relationship of the switching waveforms based on the Ldi/dt voltage drop resulted from the stray inductance has been reported but it is only effective

Manuscript received August 24, 2020; revised November 5, 2020; accepted December 4, 2020. Date of publication December 10, 2020; date of current version March 5, 2021. This work was supported in part by the National Nature Science Foundation of China under Grant 51807183, in part by the Science and Technology Major Project in Sichuan under Grant 2019YFG0386, and in part by the Aircraft Swarm Intelligent Sensing & Cooperative Control Key Laboratory of Sichuan Province. Recommended for publication by Associate Editor A. Lindemann. *(Corresponding author: Shan Yin.)*

Minghai Dong, Hui Li, and Yingzhe Wu are with the School of Aeronautics & Astronautics, University of Electronic Science and Technology of China, Chengdu 611731, China (e-mail: minh@std.uestc.edu.cn; kelly.li@126.com; microuestc@163.com).

Shan Yin is with the Microsystem & Terahertz Research Center, China Academy of Engineering Physics, Chengdu 610200, China, and also with the Institute of Electronic Engineering, China Academy of Engineering Physics, Mianyang 621999, China (e-mail: yinshansamuel@gmail.com).

Kye Yak See is with the School of Electrical & Electronic Engineering, Nanyang Technological University, Singapore 639798, Singapore (e-mail: ekysee@ntu.edu.sg).

Color versions of one or more figures in this article are available at https://doi.org/10.1109/TPEL.2020.3043801.

Digital Object Identifier 10.1109/TPEL.2020.3043801

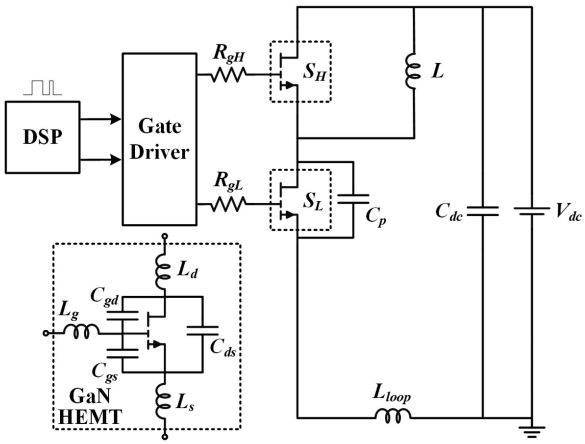

Fig. 1. Schematic of DPT circuit.

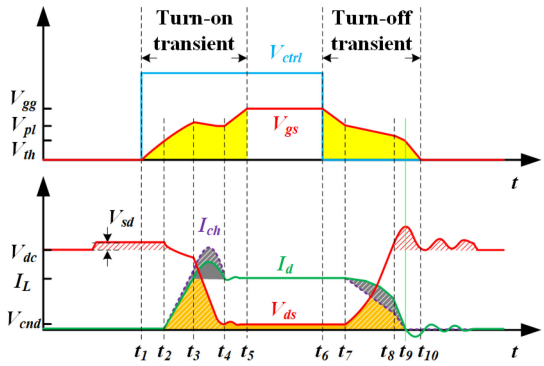

Fig. 2. Switching waveforms.

for sufficiently high load current [25]. Another reported work in [26] removes the freewheeling diode and load inductor and replaced them with a precision 100-Ω resistor with low parasitic inductance, which results in no phase shift between voltage and current waveforms alignment but the use external auxiliary circuit can be rather complex.

To overcome the aforementioned constraints, this article proposes a novel postprocessing method to estimate the switching loss accurately based on the DPT method. A postprocessing deskew technique for GaN devices is adopted. It consists of three parts, the wavelet denoising process, the $V-I$ alignment process, and the linear interpolation process. First, to effectively reduce the error from background noise, the wavelet shrinkage is included in the wavelet denoising process. Then, based on the theoretical switching characteristics of GaN devices, the reference points of the switching waveform can be established so that the propagation delay of the probe could be eliminated during the $V-I$ alignment process. Finally, the linear interpolation process is applied to improve the alignment resolution.

The rest of this article is organized as follows. Section II provides an overview of the theoretical loss mechanism of GaN HEMT. Section III develops a modified SPICE model of a commercial GaN HEMT EPC2014 to include the effects of parasitic elements in the switching loss. Next, a switching loss estimation method based on the proposed postprocessing technique is described in details in Section IV. Section V elaborates the DPT experiment setup for the GaN HEMT and Section VI validates the proposed loss estimating method experimentally. Finally, Section VII concludes this article.

II. Loss Mechanism of GaN Devices

For the DPT circuit shown in Fig. 1, the loss mechanism of low-side GaN HEMT (S_L) will be analyzed to provide the *a priori* knowledge for the proposed method. L_{loop} is the power loop inductance of printed circuit board (PCB). C_p is the PCB parasitic capacitance. R_{gx} is external gate resistance. L is the load inductance. C_{dc} is dc-link capacitance, and V_{dc} is dc-bus voltage. C_{gs}, C_{gd}, and C_{ds} are the gate–source, gate–drain, and drain–source junction capacitances, respectively. L_g, L_d, and L_s are the gate, drain, and source packaging inductances, respectively. The losses can be further classified into the turn-ON loss, the turn-OFF loss and the conduction loss, which will be discussed in details in the following sections. Definitions of these losses are based on switching waveforms illustrated in Fig. 2, where V_{ctrl}, V_{gs}, V_{ds}, I_{ch}, I_d are the control signal, gate–source voltage, drain–source voltage, 2DEG channel current, and drain current, respectively. In addition, parameter symbols of S_H are marked with an additional subscript "1". It should be mentioned that due to the zero Q_{rr} property of GaN devices, there will be no reverse recovery loss E_{rr}. Although some literatures [11] have reported there is another type of loss referred to the output capacitance hysteresis, which is not considered in this article, because it only appears under very high-frequency (such as radio-frequency) application. Moreover, the impact of ringing on switching losses can be neglected, as it only contributes an insignificant part of the total loss [27].

A. Loss During Turn-ON Transition

According to switching waveforms given in Fig. 2, the turn-ON transition of S_L can be subdivided into four stages, the turn-ON delay, the current commutation, the voltage commutation, and the current ringing. Each of these stages will be described in details to present the loss mechanism in the turn-ON transition. It includes the turn-ON $V-I$ overlapping loss $E_{\text{vi,on}}$ (orange zone with white stripe), the capacitor self-charging/discharging loss E_{oss} (gray zone with white stripe), the capacitor charging loss E_{qoss} (gray zone), the reverse conduction loss E_{sd} (white zone with red stripe), the forward conduction loss E_{cond} (orange zone), and the gate drive loss E_{gdv} (yellow zone). E_{cond} and E_{gdv} are not considered here for ease of analysis.

1) Stage 1 (Turn-ON Delay, $t_1 \sim t_2$): When the control signal V_{ctrl} becomes high, the gate driver charges the input capacitance C_{iss} with a gate current I_g and V_{gs} rises. Since the value of V_{gs} is below the gate threshold voltage V_{th}, S_L works in the cut-off region and its 2DEG channel is not conducted. Meanwhile, S_H is still in the reverse conduction, and therefore, losses in this stage only contribute to E_{sd}.

2) Stage 2 (Current Commutation, $t_2 \sim t_3$): V_{gs} increases exponentially and exceeds V_{th}, and S_L enters the saturation region. The 2DEG channel starts to conduct, and the inductor current is transferred from S_H to S_L. Thus, E_{sd} still exists in

this stage and I_d is given by

$$I_d = g_m(V_{\text{gs}} - V_{\text{th}}) \tag{1}$$

where the transconductance g_m can be extracted from the transfer characteristics. The rise of I_d leads to a voltage drop across S_L due to the effect of stray inductance ($L_{\text{stray}} = L_{d1} + L_{s1} + L_d + L_s + L_{\text{loop}}$) and V_{ds} is given by

$$V_{\text{ds}} = V_{\text{dc}} + V_{\text{sd}} - L_{\text{stray}}\frac{dI_d}{dt} \tag{2}$$

where V_{sd} is the reverse conduction voltage drop. C_{ds} discharges and V_{ds} falls, meanwhile, C_{gs} is charged by the current I_g continuously. Therefore, the increase of V_{gs} and decrease of V_{ds} lead to an increase of V_{gd}, thus charging C_{gd}. Since the 2DEG channel already conducts in this stage, the discharging current of C_{ds} and the charging current of C_{gd} will flow through the channel and the channel current I_{ch} is given by

$$I_{\text{ch}} = I_d + C_{\text{oss}}\frac{dV_{\text{ds}}}{dt} + C_{\text{gd}}\frac{dV_{\text{gd}}}{dt} \tag{3}$$

where C_{oss} is the output capacitance and given by $C_{\text{oss}} = C_{\text{gd}} + C_{\text{ds}}$. Considering $C_{\text{gd}} \ll C_{\text{ds}}$ and $dV_{\text{gs}}/dt \ll dV_{\text{ds}}/dt$, the last term of (3) can be neglected. The first and second terms contribute to $E_{\text{vi,on}}$ and E_{oss}, respectively. Apart from C_{oss}, C_p also contributes to E_{oss}, which is voltage-independent [28] and is introduced by adjacent coppers [29], which can be extracted by the finite-element method (FEM) simulation. Since L_d and L_s of S_L are very small, C_{oss} and C_p can be combined into the equivalent capacitance C_{eq}. Thus, (3) can be simplified to

$$I_{\text{ch}} = I_d + C_{\text{eq}}\frac{dV_{\text{ds}}}{dt}. \tag{4}$$

In summary, this stage contributes to losses E_{sd}, $E_{\text{vi,on}}$, and E_{oss}.

3) Stage 3 (Voltage Commutation, $t_3 \sim t_4$): When I_d reaches the load current I_L and continues to rise, it leads to the further fall of V_{ds}. V_{gs} equals Miller plateau voltage V_{pl}. Similar to the analysis of stage 2, the voltage drop across C_{gs} reaches a dynamic balance while C_{gd} shunts the majority of charging current and increases nonlinearly, and V_{ds} drops, which is given by

$$V_{\text{ds}} = V_{\text{dc}} - V_{\text{ds1}} - L_{\text{stray}}\frac{dI_d}{dt} \tag{5}$$

where V_{ds1} is the drain–source voltage of S_H. Since the 2DEG channel of S_L is already conducting, the rest of self-discharging current of C_{eq} will flow into the 2DEG channel of S_L, which contributes to E_{oss}. Meanwhile, as the 2DEG channel (reverse biased) of S_H is already cut off, the charging current of C_{oss1} will flow through S_L and generate a current bump, which is the source of E_{qoss}, as shown in Fig. 3(a). Since this current bump is mixed with I_d, E_{qoss} is considered as part of $E_{\text{vi,on}}$ to simplify the analysis and I_d is now given by

$$I_d = I_L + C_{\text{oss1}}\frac{dV_{\text{ds1}}}{dt} \tag{6}$$

and I_{ch} is the same as in (4). To summarize, this stage contributes to losses $E_{\text{vi,on}}$ and E_{oss}.

It should be noted that the voltage commutation can be eliminated in stage 3 under the extreme condition of low dc-bus voltage and large stray inductance. It can be explained by (2) that a large L_{stray} leads to last term comparable to V_{dc} and V_{ds} may drop to zero in stage 2. $E_{\text{vi,on}}$ disappears in stage 3 since there is no $V - I$ overlapping. Also, E_{oss} will be fully dissipated in stage 2. The derivation of turn-ON energy under extreme situation is given in the Appendix. Under the extreme condition, for example, $V_{\text{dc}} = 18$ V and $L_{\text{stray}} = 12.25$ nH, $di/dt = 2.51$ kA/μs, the calculated energy is 33.49 nJ, which is quite close to the measured result (28.98 nJ).

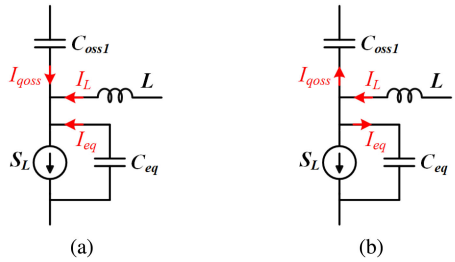

Fig. 3. Simplified circuit diagrams of current sharing in voltage commutation. (a) Turn-ON transition. (b) Turn-OFF transition.

4) Stage 4 (Current Ringing, $t_4 \sim t_5$): The 2DEG channel is fully conducted. S_L enters the ohmic region and becomes resistive in this stage [30]. I_g continues to charge C_{gd} and V_{gs} finally reaches the driving voltage V_{gg}. This stage is also known as current ringing stage because of the resonance caused by C_{eq} and L_{stray}. As mentioned earlier, the loss contributed by ringing can be neglected and only the conduction loss E_{cond} is considered in this stage.

B. Loss During Turn-OFF Transition

Similar to the turn-ON transition, the turn-OFF transition can be subdivided into four stages: 1) the turn-OFF delay, 2) the voltage commutation, 3) the current commutation, and 4) the voltage ringing stages. The loss during this transition is normally smaller than that of turn-ON transition, and can be classified as soft-switching [31]. The mechanism of losses $E_{\text{vi,off}}$, E_{oss}, and E_{sd} during turn-OFF transition will be discussed as follows.

1) Stage 5 (Turn-OFF Delay, $t_6 \sim t_7$): When V_{ctrl} becomes low, C_{gs} discharges and V_{gs} begins to fall. At the beginning of this stage, S_L is still in the ohmic region and its 2DEG channel is fully conducted. I_d and V_{ds} can be regarded as nearly constant, and therefore, this stage contributes to E_{cond} only.

2) Stage 6 (Voltage Commutation, $t_7 \sim t_8$): V_{gs} continues to fall and reaches the Miller plateau. S_L enters into the saturation region. In contrast to stage 3, C_{eq} is charging, whereas C_{oss1} is discharging, as shown in Fig. 3(b). V_{ds}, I_d, and I_{ch} are expressed, respectively, as follows:

$$V_{\text{ds}} = V_{\text{dc}} + V_{\text{ds1}} + L_{\text{stray}}\frac{dI_d}{dt} \tag{7}$$

$$I_d = I_L - C_{\text{oss1}}\frac{dV_{\text{ds1}}}{dt} \tag{8}$$

$$I_{\text{ch}} = I_d - C_{\text{eq}}\frac{dV_{\text{ds}}}{dt}. \tag{9}$$

It is found that C_{oss1} leads to a current knee and, thus, a reduction of turn-OFF $V-I$ overlapping loss $E_{vi,off}$. Since the charging current of C_{eq} is from the external current source instead of the 2DEG channel, the power dissipation is not contributed by the device. This stage ends when S_H starts to conduct reversely. In summary, this stage contribute to $E_{vi,off}$.

3) Stage 7 (Current Commutation, $t_8 \sim t_9$): As V_{ds} increases beyond $V_{dc}+V_{sd}$ due to the effect of stray inductance and reverse voltage drop of S_H, C_{eq} continues to be charged by I_d. Thus, I_d continues to fall to zero with the correlation shown in (1), and I_{ch} is the same as (9) and V_{ds} is given by

$$V_{ds} = V_{dc} + V_{sd} + L_{stray}\frac{dI_d}{dt}. \tag{10}$$

Losses in this stage contribute to E_{sd} and $E_{vi,off}$. At the end of stage 7, I_{ch} and I_d drops to zero since $V_{gs}=V_{th}$. Meanwhile, V_{ds} reaches to its peak. This relationship is useful to locate the alignment point to calibrate the propagation delay of voltage and current probes, and will be discussed in the following section.

Similar to the analysis in stage 3, the current commutation in this stage can be neglected under the extreme condition of low load current and large C_{eq} as explained by (8) and (9), I_{ch} may drop to nearly zero in stage 6. Thus, there is no $E_{vi,off}$ in stage 7 as there is no $V-I$ overlapping. The analysis agrees well with the previous work in [32], where the turn-OFF transient waveforms are divided into three cases.

4) Stage 8 (Voltage Ringing, $t_9 \sim t_{10}$): In this stage, S_L is in the cut-off region due to the continuous discharge of C_{gs}, thus V_{gs} is below V_{th}. This stage is also known as voltage ringing stage due to the resonance caused by C_{eq} and L_{stray}. Compared with the current ringing in stage 4, the voltage ringing is more significant since it is less damped with 2DEG channel open, which also leads to significant current ringing with the expression given by

$$I_d = C_{eq}\frac{dV_{ds}}{dt}. \tag{11}$$

It can be found the phase of V_{ds} lags that of I_d by 90°.

C. Switching Loss in Measurement

Based on the earlier analysis, it can be concluded that the theoretical total loss E_{tt} is given by

$$E_{tt} = E_{ton} + E_{toff} \tag{12}$$

where the theoretical turn-ON and turn-OFF losses, E_{ton} and E_{toff}, are due to the overlapping between the waveforms of V_{ds} and I_{ch}, and are expressed as

$$\begin{cases} E_{ton} = \int_{t_2}^{t_4} V_{ds} I_{ch} dt = E_{vi,on} + E_{oss} \\ E_{toff} = \int_{t_7}^{t_9} V_{ds} I_{ch} dt = E_{vi,off} \end{cases} \tag{13}$$

and E_{oss} can be derived from the energy balance theory that the energy stored in the turn-OFF transition will be fully dissipated in the turn-ON transition through the 2DEG channel of GaN HEMT, as given by

$$E_{oss} = \int_0^{V_{dc}+V_{sd}} V_{ds} C_{oss} dV_{ds}. \tag{14}$$

As measuring I_{ch} is impossible and only I_d can be measured in the DPT experiment, which leads to an error in the switching loss. The measured turn-ON and turn-OFF losses, E_{mon} and E_{moff}, are given by

$$\begin{cases} E_{mon} = E_{vi,on} \\ E_{moff} = E_{vi,off} + E_{oss} \end{cases} \tag{15}$$

and the measured total loss E_{mt} is given by

$$E_{mt} = E_{mon} + E_{moff} = E_{tt}. \tag{16}$$

Based on the previous equations, it can be found that E_{oss} is measured as part of E_{moff}, whereas it is part of E_{ton}. It is because that the discharging current of C_{oss} and C_p flows through the 2DEG channel and cannot be measured. Fortunately, the same amount of E_{oss} can be measured in the turn-OFF transition. Thus, the measured total loss is the same as that of the theoretical derivation. For simplicity, in the rest of this article, E_{mon} and E_{moff} are denoted as E_{on} and E_{off}, respectively.

III. Impact of PCB Parasitic Elements on Switching Loss

The fast switching speed makes GaN HEMTs highly sensitive to the PCB parasitic elements, which is the cause of most electromagnetic interference (EMI) issues. The ringing affects the measured waveforms and if the voltage spike at turn-OFF is high enough, it may even lead to the avalanche breakdown. In addition, as the switching loss is estimated based on $V-I$ overlapping, it may also influence the accuracy of the estimated switching loss. Therefore, this section proposes a modified SPICE model to include the influence of L_{stray} and C_p in the loss estimation. Based on the proposed model, the relationship between the parasitic elements and the switching loss can be analyzed with the parasitic elements as varying parameters.

A. Modified SPICE Model

To assess the influence of parasitic elements, a SPICE model of GaN HEMT EPC2014 is modified based on the device model from manufacturer [33]. In this model, the relationship between V_{ds} and I_d is given by

$$I_d = \frac{k_1 \ln\left(1+\exp\left((V_{gs}-k_2)/k_3\right)\right) V_{ds}}{1+\max((k_4+V_{gs}),k_5)V_{ds}} \tag{17}$$

where parameters k_x ($x=1,2,\ldots,5$) can be obtained through curve fitting with the electrical characteristic of the device given in the datasheet [34]. The three junction capacitances (C_{gs}, C_{gd}, C_{ds}) are voltage-dependent and can be expressed in terms of the following function:

$$C_x(V) = P_{1x}\ln\left(P_{2x}+\exp\left((V+P_{3x})/P_{4x}\right)\right)+P_{5x}. \tag{18}$$

With (18), the three junction capacitances are described by

$$\begin{cases} C_{gs} = C_{a1}(V_{gs}) + C_{a2}(V_{ds}) \\ C_{gd} = C_{b1}(V_{gs}) + C_{b2}(V_{gd}) + C_{b3}(V_{gd}) \\ C_{ds} = C_{c1}(V_{ds}) + C_{c2}(V_{ds}) \end{cases} \tag{19}$$

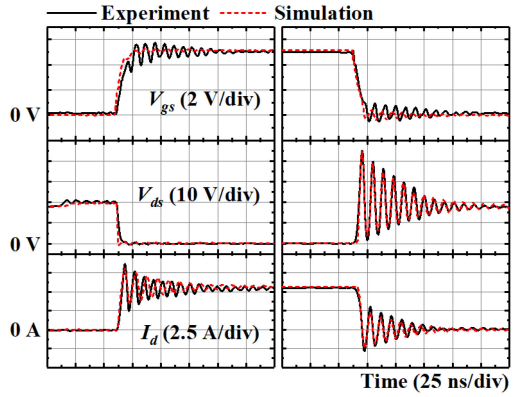

Fig. 4. Switching waveforms comparison between experiment (black solid line) and simulation (red dashed line) when $L_{\text{loop}} = 12.25$ nH, $C_p = 1$ pF.

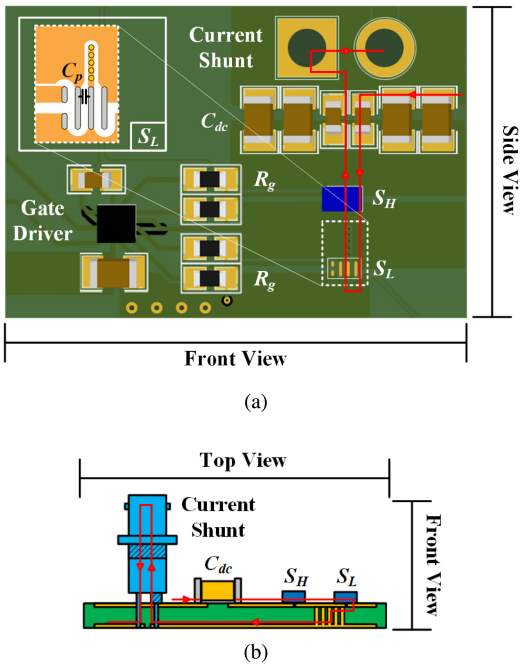

Fig. 5. Low-parasitic PCB design and power loop (red line) of DPT circuit for GaN HEMT. (a) Top view. (b) Side view.

where the respective terms can be obtained from $C - V$ curve of the datasheet.

To validate the modified SPICE model, it is tested in a DPT circuit with the configuration same as the experiment ($R_g = 10\ \Omega$, $V_{\text{dc}} = 18$ V, $I_L = 6$ A, and $L = 31\ \mu$H). L_{loop} is extracted from (20) and found to be 12.25 nH and C_p is extracted by FEM and found to be 1 pF. The comparisons between simulated and measured switching waveforms of V_{gs}, V_{ds}, and I_d are shown in Fig. 4. It is found that the measured and simulated results show good agreement.

B. Impact of Stray Inductance

The total stray inductance in a DPT circuit consists of packaging inductances of GaN device, decoupling capacitor, and the parasitic inductance of PCB, as shown in Fig. 5. With the advanced packaging technology such as land grid array [35],

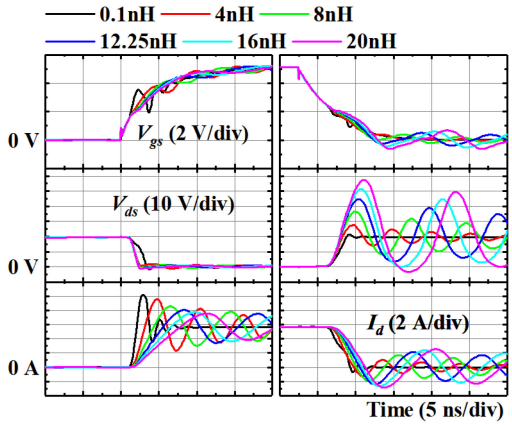

Fig. 6. Simulated switching waveforms with variation of L_{loop} (0.1−20 nH) at $C_p = 1$ pF.

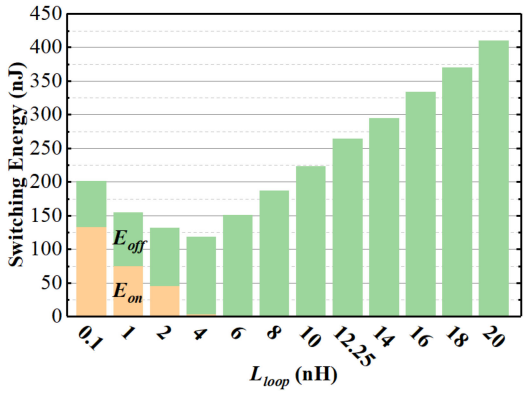

Fig. 7. Simulated switching losses during turn-ON and turn-OFF transitions with varying L_{loop} (0.1−20 nH) at $C_p = 1$ pF.

the packaging inductance can be as low as 0.1 nH. The packaging inductance contributed by the decoupling capacitor can be minimized by using several surface mounted device ceramic capacitors in parallel. Thus, the PCB parasitic inductance L_{loop} dominates L_{stray}. The value of L_{loop} can be estimated from the resonant frequency at the switching transition given by

$$L_{\text{loop}} = \frac{1}{C_{\text{eq}} (2\pi f_s)^2} - L_{\text{pkg}} \tag{20}$$

where the total packaging inductance L_{pkg} is estimated to be 0.2 nH.

The influence of different values of L_{loop} on the switching loss is further investigated by varying it from 0.1 to 20 nH to cover good to bad PCB layout design. As expected, Fig. 6 shows that higher L_{loop} has a strong impact on the switching waveforms, which decreases di/dt and increases dv/dt at both turn-ON and turn-OFF transitions. During the turn-ON transition, V_{ds} directly drops to zero before I_d rise to I_L, which means the stage 3 can be partially or fully eliminated. Thus, E_{on} decreases with the increase of L_{loop}. During the turn-OFF transition, the fast voltage slew rate and slow current slew rate, together with the high-voltage spike, increase E_{off} significantly.

Fig. 7 shows the breakdown of switching losses during turn-ON and turn-OFF with varying L_{loop}. When $L_{\text{loop}} = 0.1$ nH, E_{on} is 133.5 nJ, which is larger than $E_{\text{off}} = 67.3$ nJ. With higher

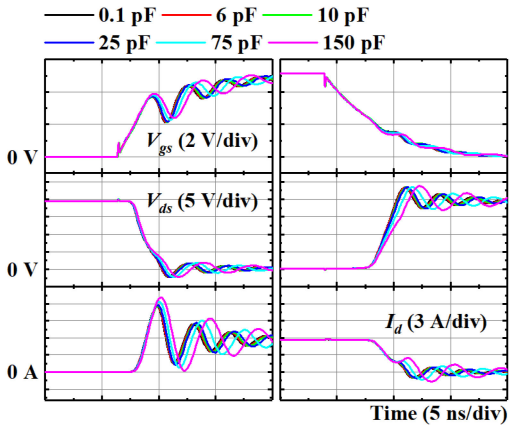

Fig. 8. Simulated switching waveforms with varying C_p (0.1−150 pF) at $L_{\text{loop}} = 1$ nH.

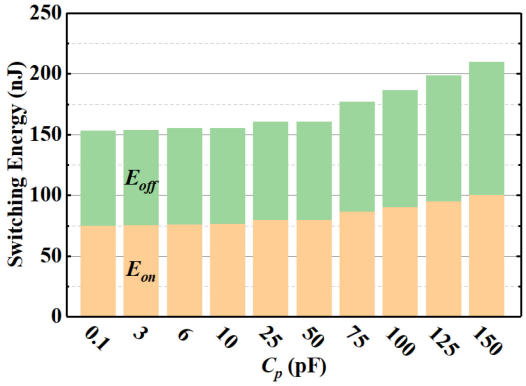

Fig. 9. Simulated switching losses during turn-ON and turn-OFF transitions with varying C_p (0.1−150 pF) at $L_{\text{loop}} = 1$ nH.

L_{loop}, E_{off} further increases and E_{on} becomes negligible, which agrees well with the findings in [4]. Based on Fig. 7, it reveals that there is an optimal L_{loop} to achieve minimum total switching loss and highest conversion efficiency. Hence, the lowest L_{loop} is not always desired, especially for soft-switching application.

C. Impact of Parasitic Capacitance

With the increase of switching frequency and more PCB layers, loss from the parasitic capacitance can no longer be neglected [36]. As shown in Fig. 1, C_p is antiparallel with S_L, thus it requires additional current to complete the charging and discharging processes. This additional loss contributes to E_{oss} and it has to be evaluated separately.

By varying C_p from 0.1 to 150 pF, its influence on the switching waveforms is investigated, as shown in Fig. 8. Higher C_p increases di/dt and decreases dv/dt. During the turn-ON transition, I_d rises to I_L before V_{ds} drops to zero, thus E_{on} increases with the increase of C_p. During the turn-OFF transition, I_d drops at first and then rises up. The reason for the changes on I_d is due to the charging of C_{oss} and C_p. This current bump results in an increase of E_{off}.

The breakdown of switching losses during turn-ON and turn-OFF transitions with varying C_p is shown in Fig. 9. When C_p is 0.1 pF, E_{on} is 75.5 nJ, and E_{off} is 77.6 nJ. When C_p is 150 pF, which is close to C_{oss}, E_{on} is 100.8 nJ, and E_{off} is 108.7 nJ. Further increase in C_p, the incremental changes of both E_{on} and E_{off} are almost the same. Interestingly, it is found that even when C_p increases to 10 pF, the switching loss shows a slight difference compared with that at 0.1 pF. Hence, the influence of C_p can be neglected for the 2-layer PCB design in this article.

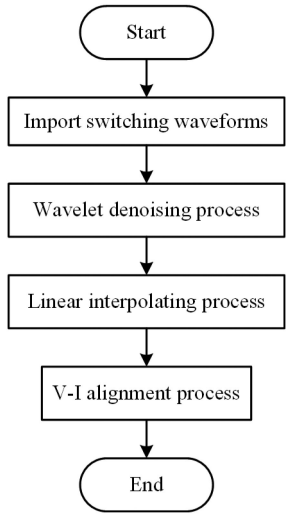

Fig. 10. Flowchart of postprocessing deskew method.

IV. Postprocessing-Technique-Based Switching Loss Estimation Method

This section presents a postprocessing method to deskew switching waveforms, which are obtained from the DPT experiment. First, the test setup is introduced and issues that can impact the measurement accuracy are discussed. Then, the mechanism of postprocessing technique is illustrated, with the flowchart shown in Fig. 10. To better understand the proposed method, three processes: $V - I$ alignment, wavelet denoising, and linear interpolating processes are described in accordance with the sequence shown in Fig. 10. The $V - I$ alignment process based on the switching characteristics discussed in Section II will be described first. Then, the influence of oscilloscope background noise on the loss estimation is minimized based on a wavelet denoising technique. Finally, linear interpolating algorithm is applied to further reduce the alignment error due to the limitation of sampling rate.

A. Basic Principle

The DPT method is the most widely adopted measurement setup to estimate the switching loss. Differing from the conventional DPT, which uses a chopper circuit, the synchronous DPT is a half-bridge (HB) configuration with two complimentary gate driving signals to simulate the synchronous operating mode, as shown in Fig. 1. The value of main components including the load inductance L and the dc-link capacitance C_{dc} must be carefully chosen to ensure that the dc-link voltage V_{dc} and load current I_L are constant during the switching transition. The gate driver circuit has to be carefully designed to capitalize the high-speed capability of GaN devices. These designs are crucial

for the DPT circuit and have been well reported and will not be repeated here [20]. In the layout design, the vertical loop (red line in Fig. 5) is adopted to benefit from magnetic flux self-cancellation to reduce L_{loop} [37].

Oscilloscope and probe selections are equally important, as the bandwidth of the measurement system ($\text{BW}_{-3\text{dB}}$) is directly affected by the oscilloscope $\text{BW}_{-3\text{dB}(Sp)}$ and the probe $\text{BW}_{-3\text{dB}(Pb)}$, the system bandwidth is governed by

$$\text{BW}_{-3\text{dB}} = \frac{1}{\sqrt{\frac{1}{\text{BW}^2_{-3\text{dB}(Sp)}} + \frac{1}{\text{BW}^2_{-3\text{dB}(Pb)}}}}. \tag{21}$$

Due to the fast switching speed of GaN HEMT, any propagation delay of the measurement system can contribute toward measurement errors. Usually, it can be minimized with a short cable [38].

Besides, the parasitic elements introduced by the probes have to be taken into account for the measurement of GaN HEMT. The voltage probe with the lowest possible coupling capacitance and shortest ground lead length should be selected. The current measurement is usually the challenge when comparing with the voltage measurement, as the current probe has to be inserted into the power loop, which increases L_{loop}. The conventional current transformer and Rogowski-coil are not suitable due to their relatively large size. The current surface probe method [39] and integrated current measurement method [40] have superior performance but at the expense of complexity and higher costs. As a compromise, the current shunt is chosen for the experiment.

B. $V - I$ Alignment Process

Considering the high switching speed of GaN HEMTs, any slight propagation delay between the voltage and current probes can contribute to large measurement error. Although the oscilloscope provides the sampling synchronization between voltage probes (refer to Fig. 13), the synchronization between voltage and current probes are challenging without the use of external deskewing. Thus, the need for postprocessing alignment is required.

The first step of this process is to locate a suitable point based on the switching mechanism. Based on the discussion in the Section II, t_9 (i.e., end of stage 7 and beginning of stage 8) is selected as the alignment point, as shown in Fig. 2. At this point, V_{ds} reaches the peak value, thus $dV_{\text{ds}}/dt = 0$. From (9), it can be found that $I_{\text{ch}} = I_d$. Considering the phase of V_{ds} that lags that of I_d by 90° during the voltage ringing stage, it can be referred that $I_{\text{ch}} = I_d = 0$ at t_9. Thus, V_{gs} should be equal to V_{th} so that the 2DEG channel is in cut-off. Bearing in mind that V_{th} is temperature-dependent, the alignment point for V_{gs} should take the temperature effect into consideration, as shown in Fig. 11. To summarize, the alignment point is selected to be t_9 with $V_{\text{ds}} = V_{\text{dsmax}}$, $V_{\text{gs}} = V_{\text{th}}$, and $I_d = 0$. The alignment point t_9 is complementary to t_2 at the turn-ON transition. However, t_9 is much easier to be located since the voltage and current ringings are inevitable due to the effect of L_{stray}.

The $V - I$ alignment process can be implemented in MATLAB with its flowchart shown in Fig. 12. First, the three measured signal data $x(n) = [V_{\text{ds}}, V_{\text{gs}}, I_d]^T$ are imported. Then, the

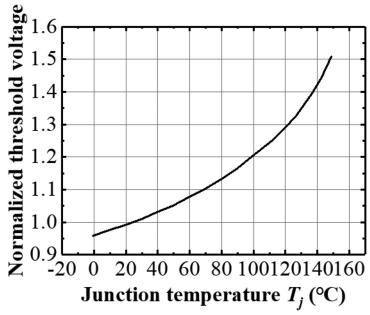

Fig. 11. Relationship between V_{th} and junction temperature T_j of GaN HEMT EPC2014 when I_d is 2 mA.

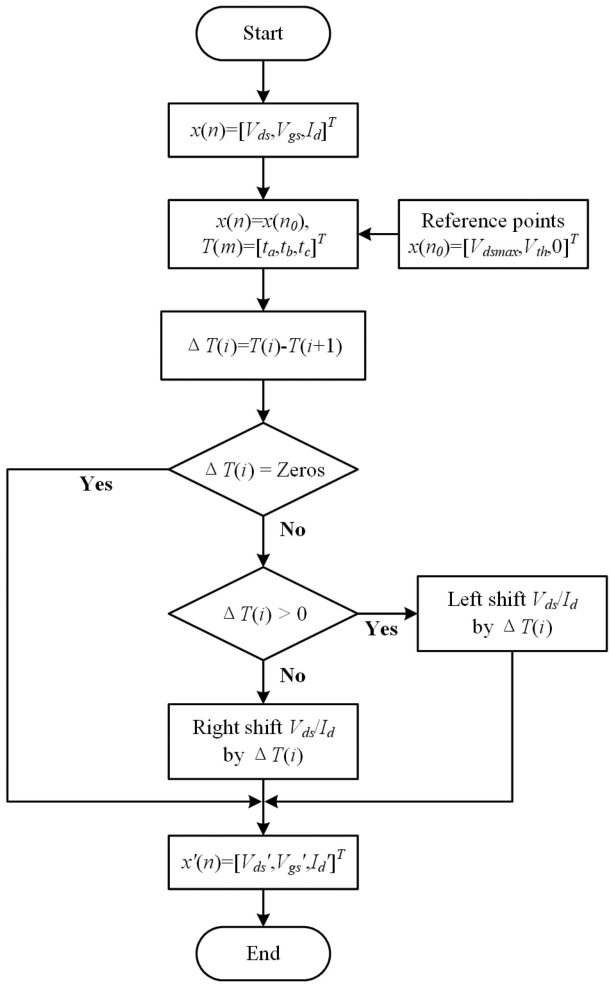

Fig. 12. Flowchart of $V - I$ alignment process.

reference points t_a, t_b, and t_c at $V_{\text{ds}} = V_{\text{dsmax}}$, $V_{\text{gs}} = V_{\text{th}}$, and $I_d = 0$ are obtained, respectively. By comparing these reference points, the time differences can be determined as

$$\Delta T(i) = T(i) - T(i+1) \tag{22}$$

where i is chosen as 1 or 2 for representation of $V_{\text{ds}} - V_{\text{gs}}$ or $V_{\text{gs}} - I_d$ probe alignment. If $\Delta T(i) > 0$, it indicates that V_{ds} (I_d) probe has a propagation delay and it should be shifted left with respected to V_{gs} by the time difference $\Delta T(i)$. Similarly,

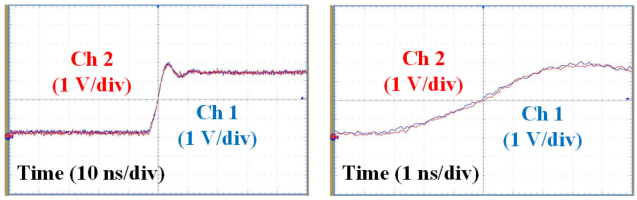

(a) (b)

Fig. 13. Background noise on measured waveforms observed on the oscilloscope at different time scale using the voltage probe TDP1000 at channel 1 and 2. (a) 10 ns/div. (b) 1 ns/div.

it should be shifted right if $\Delta T(i) < 0$. The process continues till $\Delta T(i) = 0$ and finally, the alignment of the signals $x(n) = [V'_{\rm ds}, V'_{\rm gs}, I'_d]^T$ is obtained.

C. Wavelet Denoising Process

The measured signals from the digital oscilloscope are always mixed with noises. Fig. 13 illustrates the undesirable random zig-zag noises mixed with the desired voltage signals. The noise is contributed by the front-end analog conditioning circuit thermal noise, quantization noise in analog-to-digital converter (ADC), etc. Since the proposed loss estimation method is based on the measured waveforms, the noise may not only make the $V - I$ alignment more difficult but also affect the accuracy of the loss estimation. Therefore, the influence of the noise must be reduced. These noises can be modeled as Gaussian white noises, which can be reduced by the wavelet denoising technique. For the following discussion, the voltage and current signal, which are the wanted signals, will be denoted as "signal," whereas the Gaussian white noise, which is unwanted noise, will be denoted as "noise."

The denoising process is based on the wavelet transform, which overcomes shortcomings of Fourier transform. The wavelet transform uses a set of basis analysis functions known as "wavelet," and then provide a mother wavelet $\phi(t)$. By shifting and scaling, one can get a set of basis functions called as "wavelet basis," as given by

$$\phi_{a,b}(t) = \frac{1}{\sqrt{a}}\phi(\frac{t-b}{a}). \tag{23}$$

The wavelet transform is the inner product of input signal $x(t)$ and $\phi_{a,b}(t)$

$$\mathrm{WT}_x(a,b) = \int x(t)\phi^*_{a,b}(t)dt = \langle x(t), \phi_{a,b}(t)\rangle \tag{24}$$

where a is positive and defines the scale, whereas b is any real number and defines the shift. Therefore, based on the wavelet transform, the denoising process can be applied with the flowchart shown in Fig. 14. The measured waveforms $x(n) = [V_{\rm ds}, V_{\rm gs}, I_d]^T$ are defined as original waveforms

$$x(n) = s(n) + u(n) \tag{25}$$

where $s(n)$ is the signal, and $u(n)$ is the noise. By applying the wavelet transform on both sides of (25), it results in

$$\mathrm{WT}_x(a,b) = \mathrm{WT}_s(a,b) + \mathrm{WT}_u(a,b). \tag{26}$$

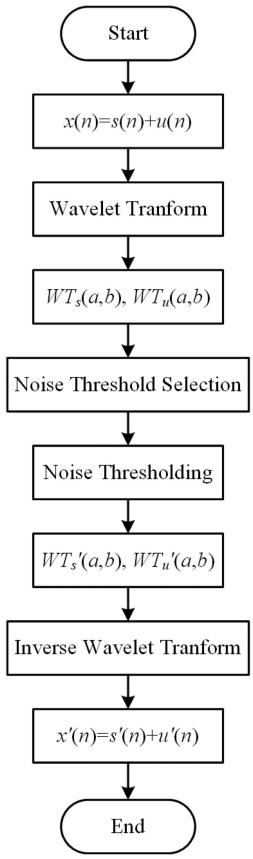

Fig. 14. Flowchart of wavelet denoising method.

Since $u(n)$ is Gaussian white noise, it still remains as the Gaussian white noise after the wavelet transform based on the signal processing theory. Therefore, the correlation of $s(n)$ is removed, and its energy is only on the wavelet coefficient, which is the maximum value of modules in all scales. Noting that $u(n)$ is still the Gaussian white noise, its wavelet coefficient is uncorrelated and distributed in each time axis of all scales. Hence, the wavelet denoising process is to keep the large coefficient unaltered and set the small coefficient to zero. Then, by applying the inverse wavelet transform, the noise can be minimized.

In reality, the small coefficient cannot be simply set to zero, as there is useful information in it. Therefore, the wavelet shrinkage is applied and the soft thresholding is selected as

$$\omega_\lambda = \begin{cases} [\mathrm{sign}\,(\omega)]\,(|\omega| - \omega)\,, & |\omega| \geq \omega \\ 0, & |\omega| < \omega \end{cases} \tag{27}$$

where ω_λ is the wavelet coefficients value imposed threshold, λ is the threshold value, and ω is the wavelet coefficient. Therefore, the key issue is how to adjust threshold to obtain the optimal threshold for the signal. To overcome this issue, the principle of Stein's unbiased risk estimate is deployed as follows:

$$\begin{cases} sx2(k) = (\mathrm{SRT}_x)^2 \\ \lambda = \sqrt{sx2\,(k_{\min})} \end{cases}, \quad k = 0, 1, \ldots, N-1 \tag{28}$$

where N is the length of signal array, $sx2(k)$ is a new signal array, SRT_x is the array of absolute value of $x(n)$ sorted from

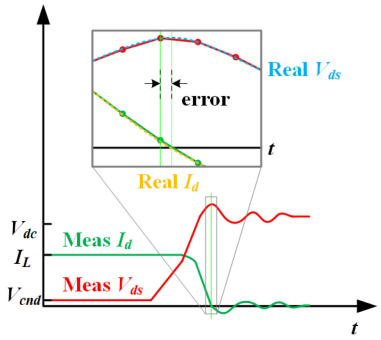

Fig. 15. Switching waveforms of $V_{\rm ds}$ and I_d in turn-OFF transition show how the fixed sampling step of oscilloscope can bring in the error.

ascending order, and $k_{\rm min}$ is the optimal point, which is given by

$$\min\left[1-\frac{2k}{N}+\frac{1}{N}\sum_{j=1}^{k}sx2(j)+\left(1-\frac{k}{N}\right)sx2\left(N-k\right)\right]. \tag{29}$$

Both (28) and (29) are implemented in the MATLAB wavelet Toolbox so that the noise can be effectively filtered and minimized.

D. Linear Interpolation Process

Even the sampling rate of advanced digital oscilloscope is in the range of 1−100 GS/s, it is still a challenging task to align precisely at the point when $V_{\rm ds} = V_{\rm dsmax}$, $V_{\rm gs} = V_{\rm th}$, and $I_d = 0$. As shown in Fig. 15, the GaN HEMT EPC2014 has a threshold voltage $V_{\rm th}$= 1.4 V. However, the nearest point to $V_{\rm th}$ is 1.43 V, which can lead to measurement error due to inability of precise alignment.

The measured signal $x(n)$ is sampled at a fixed sampling step of t_s. As t_s is usually small enough (0.2 ns for 5 GS/s in this work), the interpolation point between the two sampling points can be estimated by the linear approximation. Hence, the linear interpolation method is adopted and the linear interpolated data $x'(n)$ can be given by

$$x'(n) = x(k) + \frac{\left(x\left(k+1\right)-x(k)\right)\left(t'(n)-t(k)\right)}{t\left(k+1\right)-t(k)} \tag{30}$$

where $t(k+1)-t(k)$ is constant as t_s is a fixed value. It should be noticed that this process is before the $V-I$ alignment process, and therefore, its influence on the alignment has to be considered. For example, the time difference between $V_{\rm gs} = V_{\rm th}$ and $I_d = 0$ for one group of measured waveforms is 0.06 ns, whereas that for $V_{\rm ds} = V_{\rm dsmax}$ and $V_{\rm gs} = V_{\rm th}$ is 0.13 ns. The most straightforward way is to interpolate data for each waveform using the time steps of 0.06 and 0.13 ns. However, by doing so, it makes the sampling rate of the measured waveforms a variable, which can lead to distorted waveforms during the $V-I$ alignment process. Thus, it is better to interpolate all data by a fixed time step of $t_{\rm itp}$, which must be carefully chosen.

It is a balance between smaller time step and longer computation time. In order to select an appropriate $t_{\rm itp}$, three time points t_a, t_b, and t_c are defined, which are the nearest sampling point to $V_{\rm ds} = V_{\rm dsmax}$, $V_{\rm gs} = V_{\rm th}$, and $I_d = 0$, respectively. To simplify the analysis, t_b is taken as the reference point, and the time difference Δt is given by

$$\Delta t = \min\left(|T(k)-T(k+1)|\right) \tag{31}$$

where $T(m) = [t_a, t_b, t_c]^T$, k is chosen as either 1 or 2 to represent the time difference of $V_{\rm ds} - V_{\rm gs}$ or $V_{\rm gs} - I_d$, respectively. Then compared with the original t_s, the interpolation rate $k_{\rm itp}$ for each data interval is obtained as follows:

$$k_{\rm itp} = \frac{\Delta t}{\Delta t_s}. \tag{32}$$

Finally, the optimized $t_{\rm itp}$ is obtained by

$$t_{\rm itp} = \frac{t_s}{a^{\lceil k_{\rm itp}\rceil}} \tag{33}$$

where the value of $k_{\rm itp}$ is rounded up to an integer to avoid a rational number, and a is an integer number, which is chosen as 10 in this article. The flowchart of linear interpolation process is given in Fig. 16.

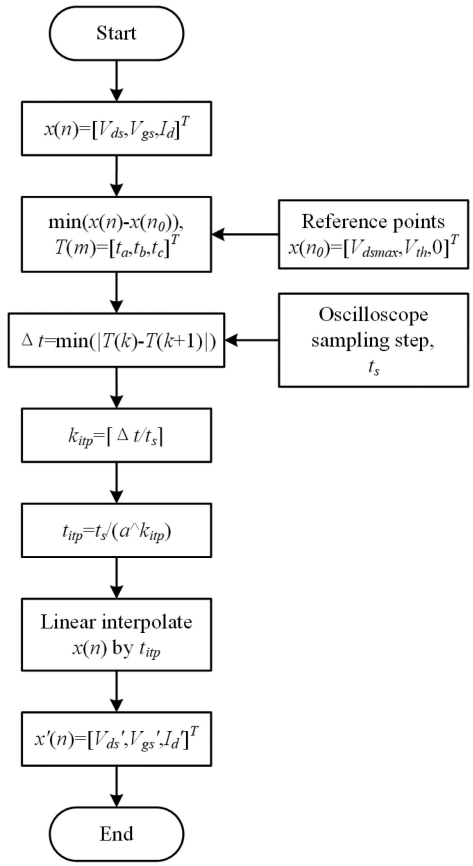

Fig. 16. Flowchart of linear interpolation process.

V. Experimental Setup

Using the GaN HEMT EPC2014 (40 V/10 A) as the device under test, DPT experimental data are collected to validate the proposed loss estimation method. The HB GaN driver LMG1205 from Texas Instruments is chosen to drive GaN HEMT. The external gate resistances for both turn-ON and turn-OFF transitions are 10 Ω. The dead time T_d is set as 50 ns to avoid the arm

TABLE I
SPECIFICATIONS OF THE DPT EXPERIMENT

Parameter	Symbol	Value
DC bus voltage	V_{dc}	18 V
Decoupling capacitance	C_{dc}	40.2 μF
Load inductance	L	31 μH
External gate resistance	R_g	10 Ω
Dead time	T_d	50 ns

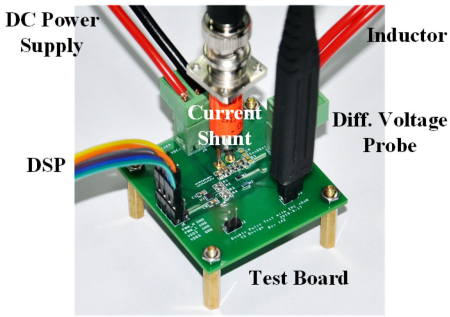

Fig. 17. Experimental setup of DPT for GaN HEMT.

shoot-through. A single-layer, air-core inductor with the value of 31 μH is used as the load to minimize the parasitic capacitance as well as to avoid the magnetic saturation. To evaluate the power dissipation at different loadings, the dc voltage is kept constant at 18 V and the load current varies from 2 to 8 A. The specifications of DPT experiment are summarized in Table I, and the experimental setup is shown in Fig. 17.

Two wideband differential voltage probes TDP1000 from Tektronix (42 V, 1 GHz) are used to measure the switching waveforms of $V_{\rm gs}$ and $V_{\rm ds}$. For the current measurement, the current shunt SDN-414-025 (bandwidth 1.2 GHz) from T&M Research is used to acquire I_d. It has a very small rise time of 0.3 ns, which has minimal influence on the current waveform. The experiment is conducted in room temperature (25 °C), where $V_{\rm th} = 1.4$ V according to Fig. 11.

VI. RESULTS AND DISCUSSION

A. Wavelet Denoising

Since the original measured waveforms from digital oscilloscope contain both signal and noise, the wavelet denoising is applied on the waveforms to filter the background noise. A comparison between the original and denoised waveforms is shown in Fig. 18. As observed in the time domain, the noise is being filtered, whereas the signal remains unaffected. From the frequency-domain results, the low-frequency (<200 MHz) components, which contain the fundamental frequency, high-order harmonics and ringing, are not influenced by the wavelet denoising. In contrast, the high-frequency (>200 MHz) components are being suppressed.

The energies associated with the switching losses, before and after the wavelet denoising process under different load current, are shown in Fig. 19. It is observed that $E_{\rm on}$ has a random relationship with the current, whereas $E_{\rm off}$ increases with the current. It can be explained as follows: The switching losses

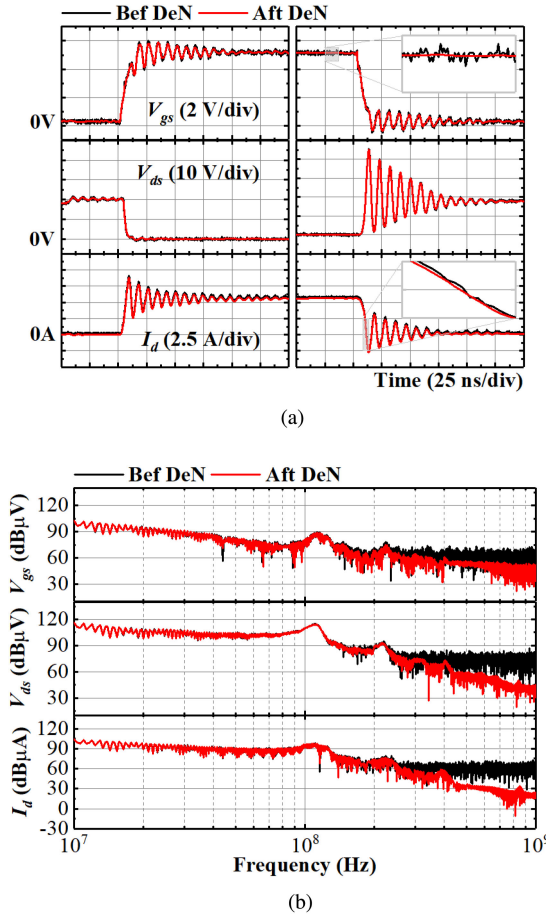

Fig. 18. Comparison of switching waveforms before (black line) and after (red line) denoising in (a) time domain and (b) frequency domain.

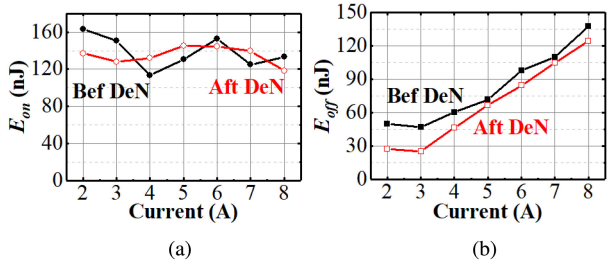

Fig. 19. Comparison of (a) $E_{\rm on}$ and (b) $E_{\rm off}$ versus load current before (black line) and after (red line) wavelet denoising process.

have two components, the actual value and the error; and the actual value of $E_{\rm on}$ is much smaller than the error but that of $E_{\rm off}$ is the reversed. In addition, $E_{\rm on} > E_{\rm off}$, which is because the $V - I$ alignment has not be conducted. The impact of Gaussian white noise on losses does not show the same tendency due to its random distribution nature.

B. $V - I$ Alignment

After the wavelet denoising process, the noise component in the signal is being cleaned up. Now the condition with a load current of 6 A is chosen for comparison to observe the effect of the alignment process, as shown Fig. 20. Since $V_{\rm gs}$ is taken as a reference signal, there are no changes before and after alignment.

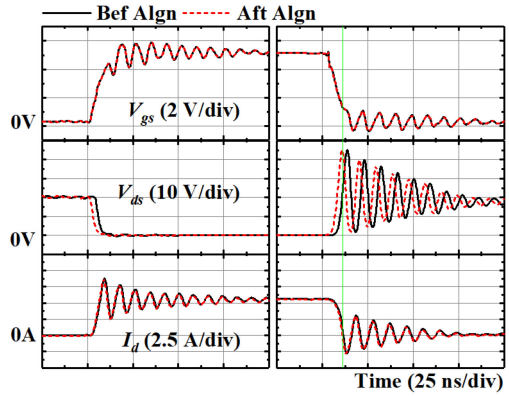

Fig. 20. Comparison of switching waveforms before (black line) and after (red dotted line) alignment with respect to the reference (light green line).

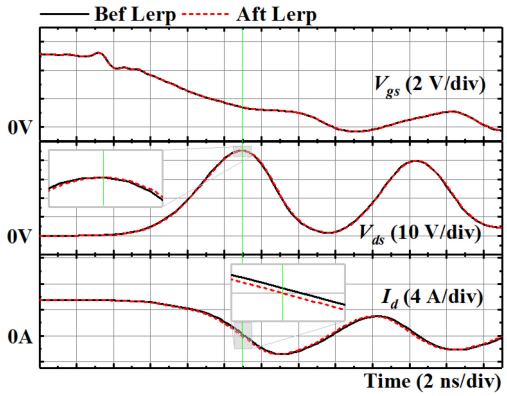

Fig. 22. Comparison of turn-OFF waveforms before (black line) and after (red dotted line) linear interpolation with respect to the reference (light green line).

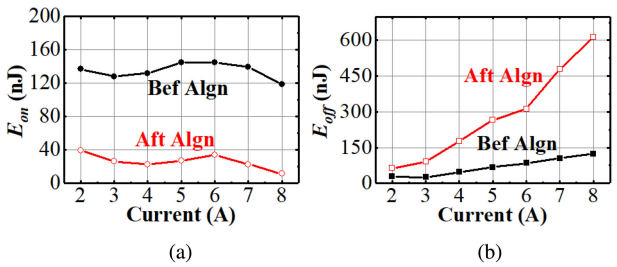

Fig. 21. Comparison of (a) E_{on} and (b) E_{off} versus load current before (black line) and after (red line) alignment process.

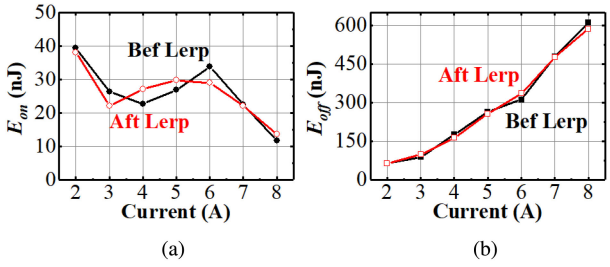

Fig. 23. Comparison of (a) E_{on} and (b) E_{off} versus load current before (black line) and after (red line) linear interpolation process.

The light green line in Fig. 20 is to show that the three signals have been correctly aligned. It is clearly observed that V_{ds} has been moved left, whereas I_d is moved slightly.

The energies associated with the switching losses before and after the alignment process under different load currents is shown in Fig. 21. It shows that E_{on} becomes lower, whereas E_{off} becomes higher, and $E_{\text{on}} < E_{\text{off}}$. It differs from the common knowledge that $E_{\text{on}} > E_{\text{off}}$. For example, when the load current is 6 A, E_{on} is decreased to 33.7 nJ from 144.6 nJ, whereas E_{off} is increased to 312.2 nJ from 84.8 nJ. It is due to the use of current shunt, which introduces a stray inductance that affects both E_{on} and E_{off}, as discussed in Section III. To summarize, the $V - I$ alignment process plays a key role of the proposed method. As it is based on the switching mechanism of GaN HEMT, this method can be easily applied.

C. Linear Interpolation

To further improve the accuracy of alignment process, a linear interpolation process is applied. Fig. 22 shows the turn-OFF waveforms before and after the linear interpolation process. Similar to the previous discussion, V_{gs} is taken as a reference signal, and a light green line is used as the reference. It is found that V_{ds} has been shifted to the right slightly, whereas I_d has been shifted to the left.

The switching energies associated with the switching losses before and after the interpolation process under different load currents are shown in Fig. 23. Comparing with the alignment process, the impact on the losses is relatively small. For example, when the load current is 6 A, E_{off} rises to 336.5 nJ from 312.2 nJ, whereas E_{on} drops to 29.0 nJ from 33.7 nJ. Since the sampling rate of oscilloscope used in this article is 5 GS/s, it has sufficient sampling rate to measure the switching waveforms of GaN HEMT.

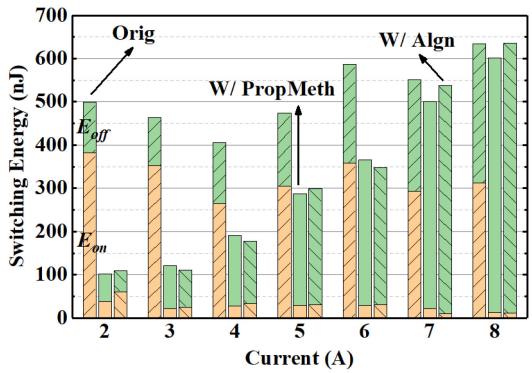

Fig. 24. Switching losses breakdown versus load current without (left) and with (middle) the proposed switching loss estimation method and only with alignment method (right).

D. Verification of Proposed Switching Loss Estimation Method

Finally, the proposed switching loss estimation method with all the three mentioned processes is implemented. Fig. 24 shows the relationship between the energies associated with the

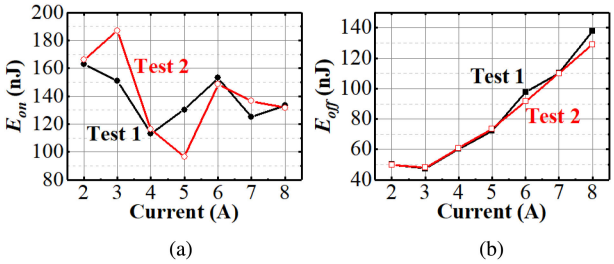

Fig. 25. Original switching energies versus load current for test 1 and test 2. (a) E_{on}. (b) E_{off}.

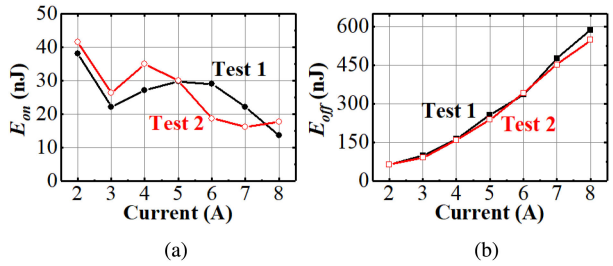

Fig. 26. Calibrated switching energies versus load current for test 1 and test 2 using the proposed method. (a) E_{on}. (b) E_{off}.

switching losses versus the load current with and without the proposed method applied. The result with only the alignment process implemented is also presented for better appreciation of the proposed method. It has shown that the original data without the postprocessing method can lead to incorrect information of the losses. For example, the zero-voltage switching (ZVS) is always preferred compared with the zero-current switching (ZCS) in the resonant converter design since $E_{\text{on}} > E_{\text{off}}$. However, for the situation with relatively large stray inductance, the selection of ZVS operation may lead to a lower conversion efficiency. Compared with the wavelet denoising and linear interpolation processes, the $V - I$ alignment process shows the highest influence on the total loss. Nevertheless, the combination of the three processes has shown a great improvement on the accuracy of the loss estimation.

To check the impact of test environment on the measured results, the proposed method is further applied to two different groups of measurement data, namely test 1 and test 2, respectively. Figs. 25 and 26 show the original and calibrated switching energies versus load current, respectively. It has shown that E_{on} is slightly different, whereas E_{off} is nearly the same between the two sets of results. It is expected because the $V - I$ overlapping for the turn-ON transition is much smaller than that of turn-OFF transition, and the measurement error will have a more significant influence.

VII. Conclusion

Starting with a comprehensive theoretical analysis of the switching mechanism and a careful evaluation of possible impact of PCB parasitic elements on the DPT measurement results, a postprocessing method has been proposed and described with the objective to estimate the switching loss of GaN HEMT accurately. The proposed method consists of three processes. The first process deals with the wavelet denoising to filter the background noise of the oscilloscope. Then, a $V - I$ alignment process is developed to reduce errors from the probes' propagation delays. Finally, the linear interpolation process is deployed to further reduce the error from the alignment due to the possible limitation of the sampling rate. Among the three processes, the $V - I$ alignment has been demonstrated to be the key factor that has the most significant impact on the accuracy of the estimated switching losses. The proposed switching loss estimation method is experimentally validated on a 40-V/10-A GaN HEMT. The proposed method provides a valuable guideline to analyze and estimate the switching losses of GaN HEMT with confidence in hard- or soft-switching GaN-based converters.

Appendix

Under the low-voltage and large stray inductance condition, only stage 2 is existed, thus E_{ton} is

$$E_{\text{ton}} = \int_{t_2}^{t_3} V_{\text{ds}} I_{\text{ch}} dt. \tag{A.1}$$

The system equations are

$$\begin{cases} I_d = g_m(V_{\text{gs}} - V_{\text{th}}) \\ V_{\text{ds}} = V_{\text{dc}} + V_{\text{sd}} - L_{\text{stray}} \frac{dI_d}{dt} \\ V_{\text{gs}} = V_{\text{gg}} - I_g R_g - L_s \frac{dI_d}{dt} \\ I_g = -C_{\text{gd}} \frac{dV_{\text{ds}}}{dt} \\ I_{\text{ch}} = I_d + C_{\text{eq}} \frac{dV_{\text{ds}}}{dt}. \end{cases} \tag{A.2}$$

Therefore, V_{ds} and I_{ch} can be obtained by

$$\begin{cases} V_{\text{ds}} = V_{\text{dc}} + V_{\text{sd}} - L_{\text{stray}} g_m \frac{dV_{\text{gs}}}{dt} \\ I_{\text{ch}} = g_m(V_{\text{gs}} - V_{\text{th}}) - C_{\text{eq}} L_{\text{stray}} g_m \frac{d^2V_{\text{gs}}}{dt^2} \\ V_{\text{gs}} = V_{\text{gg}} - C_{\text{gd}} L_{\text{stray}} g_m R_g \frac{d^2V_{\text{gs}}}{dt^2} - L_s g_m \frac{dV_{\text{gs}}}{dt} \end{cases} \tag{A.3}$$

where V_{gs}, $\frac{dV_{\text{gs}}}{dt}$ and $\frac{d^2V_{\text{gs}}}{dt^2}$ are

$$\begin{cases} V_{\text{gs}} = V_{\text{gg}} + C_1 e^{-A_1 t} + C_2 e^{-A_2 t} \\ \frac{dV_{\text{gs}}}{dt} = -C_1 A_1 e^{-A_1 t} - C_2 A_2 e^{-A_2 t} \\ \frac{d^2V_{\text{gs}}}{dt^2} = C_1 A_1^2 e^{-A_1 t} + C_2 A_2^2 e^{-A_2 t} \end{cases} \tag{A.4}$$

where

$$\begin{cases} A_1 = -\frac{L_s g_m + \sqrt{g_m(g_m L_s^2 - 4C_{\text{gd}} L_{\text{stray}} R_g)}}{2C_{\text{gd}} L_{\text{stray}} R_g g_m} \\ A_2 = -\frac{L_s g_m - \sqrt{g_m(g_m L_s^2 - 4C_{\text{gd}} L_{\text{stray}} R_g)}}{2C_{\text{gd}} L_{\text{stray}} R_g g_m} \end{cases} \tag{A.5}$$

C_1 and C_2 are constant value, which are related to the initial condition. Therefore, E_{ton} is

$$\begin{aligned}
E_{\text{ton}} &= L_{\text{stray}} V_{\text{gg}}^2 g_m^2 (t_2 - t_3) - V_{\text{dc}} V_{\text{gg}} g_m (t_2 - t_3) \\
&+ V_{\text{dc}} V_{\text{th}} g_m (t_2 - t_3) - V_{\text{gg}} V_{\text{sd}} g_m (t_2 - t_3) \\
&+ V_{\text{sd}} V_{\text{th}} g_m (t_2 - t_3) - L_{\text{stray}} g_m^2 \left(\frac{C_1^2 B_5}{2A_1} + \frac{C_2^2 B_4}{2A_2} \right) \\
&+ L_{\text{stray}} V_{\text{gg}} V_{\text{th}} g_m^2 (t_2 - t_3) + \frac{C_1 (V_{\text{dc}} + V_{\text{sd}}) g_m B_2}{A_1} \\
&+ \frac{C_2 (V_{\text{dc}} + V_{\text{sd}}) g_m B_1}{A_2} - \frac{2 C_1 L_{\text{stray}} (V_{\text{gg}} - V_{\text{th}}) g_m^2 B_2}{A_1} \\
&- \frac{2 C_2 L_{\text{stray}} (V_{\text{gg}} - V_{\text{th}}) g_m^2 B_1}{A_2} \\
&+ (A_1 C_1^2 B_5 + A_2 C_2^2 B_4) \frac{C_{\text{eq}} L_{\text{stray}}^2 g_m^2}{2} \\
&+ ((A_1^2 + A_2^2) L_{\text{stray}} C_{\text{eq}} - 2) \frac{C_1 C_2 L_{\text{stray}} g_m^2 B_3}{A_1 + A_2} \\
&+ (L_{\text{stray}} V_{\text{gg}} g_m - V_{\text{dc}}) A_1 C_1 C_{\text{eq}} L_{\text{stray}} g_m B_2 \\
&+ (L_{\text{stray}} V_{\text{gg}} g_m - V_{\text{dc}}) A_2 C_2 C_{\text{eq}} L_{\text{stray}} g_m B_1 \\
&- (A_1 C_1 B_2 + A_2 C_2 B_1) C_{\text{eq}} L_{\text{stray}} V_{\text{sd}} g_m
\end{aligned} \tag{A.6}$$

where

$$\begin{cases}
B_1 = e^{-A_2 t_2} - e^{-A_2 t_3} \\
B_2 = e^{-A_1 t_2} - e^{-A_1 t_3} \\
B_3 = e^{-A_1 t_2 - A_2 t_2} - e^{-A_1 t_3 - A_2 t_3} \\
B_4 = e^{-2A_2 t_2} - e^{-2A_2 t_3} \\
B_5 = e^{-2A_1 t_2} - e^{-2A_1 t_3}.
\end{cases} \tag{A.7}$$

REFERENCES

[1] H. Li, C. Yao, L. Fu, X. Zhang, and J. Wang, "Evaluations and applications of GaN HEMTs for power electronics," in *Proc. IEEE Int. Power Electron. Motion Control Conf.*, May 2016, pp. 563–569.

[2] M. Kasper and G. Deboy, "GaN HEMTs enabling ultra-compact and highly efficient 3kW 12V server power supplies," in *Proc. IEEE Int. Power Electron. Appl. Conf. Expo.*, Nov. 2018, pp. 1–6.

[3] B. Li *et al.*, "GaN HEMT driving scheme of Totem-Pole bridgeless PFC converter," in *Proc. IEEE Int. Power Electron. Appl. Conf. Expo.*, Nov. 2018, pp. 1–6.

[4] S. Ji, D. Reusch, and F. C. Lee, "High-frequency high power density 3-D integrated gallium-nitride-based point of load module design," *IEEE Trans. Power Electron.*, vol. 28, no. 9, pp. 4216–4226, Sep. 2013.

[5] J. Millán, P. Godignon, X. Perpiñá, A. Pérez-Tomás, and J. Rebollo, "A survey of wide bandgap power semiconductor devices," *IEEE Trans. Power Electron.*, vol. 29, no. 5, pp. 2155–2163, May 2014.

[6] D. Reusch and J. Strydom, "Evaluation of gallium nitride transistors in high frequency resonant and soft switching DC-DC converters," *IEEE Trans. Power Electron.*, vol. 30, no. 9, pp. 5151–5158, Sep. 2015.

[7] E. A. Jones, F. F. Wang, and D. Costinett, "Review of commercial GaN power devices and GaN-based converter design challenges," *IEEE J. Emerg. Sel. Top. Power Electron.*, vol. 4, no. 3, pp. 707–719, Sep. 2016.

[8] H. L. Yeo and K. J. Tseng, "Modelling technique utilizing modified sigmoid functions for describing power transistor device capacitances applied on GaN HEMT and silicon MOSFET," in *Proc. IEEE Appl. Power Electron. Conf. Expo.*, Mar. 2016, pp. 3107–3114.

[9] K. Wang, X. Yang, H. Li, H. Ma, X. Zeng, and W. Chen, "An analytical switching process model of low-voltage eGaN HEMTs for loss calculation," *IEEE Trans. Power Electron.*, vol. 31, no. 1, pp. 635–647, Jan. 2016.

[10] Y. Xin *et al.*, "Analytical switching loss model for GaN-based control switch and synchronous rectifier in low-voltage buck converters," *IEEE J. Emerg. Sel. Top. Power Electron.*, vol. 7, no. 3, pp. 1485–1495, Sep. 2019.

[11] J. Gareau, R. Hou, and A. Emadi, "Review of loss distribution, analysis, and measurement techniques for GaN HEMTs," *IEEE Trans. Power Electron.*, vol. 35, no. 7, pp. 7405–7418, Jul. 2020.

[12] J. Chen, Q. Luo, J. Huang, Q. He, and X. Du, "A complete switching analytical model of low-voltage eGaN HEMTs and its application in loss analysis," *IEEE Trans. Ind. Electron.*, vol. 67, no. 2, pp. 1615–1625, Feb. 2020.

[13] R. Hou, Y. Shen, H. Zhao, H. Hu, J. Lu, and T. Long, "Power loss characterization and modeling for GaN-based hard-switching half-bridges considering dynamic on-state resistance," *IEEE Trans. Transport. Electrific.*, vol. 6, no. 2, pp. 540–553, Jun. 2020.

[14] J. A. Anderson, C. Gammeter, L. Schrittwieser, and J. W. Kolar, "Accurate calorimetric switching loss measurement for 900 V 10 mΩ SiC MOSFETs," *IEEE Trans. Power Electron.*, vol. 32, no. 12, pp. 8963–8968, Dec. 2017.

[15] D. Rothmund, D. Bortis, and J. W. Kolar, "Accurate transient calorimetric measurement of soft-switching losses of 10-kV SiC MOSFETs and diodes," *IEEE Trans. Power Electron.*, vol. 33, no. 6, pp. 5240–5250, Jun. 2018.

[16] M. Guacci *et al.*, "On the origin of the C_{oss}-losses in soft-switching GaN-on-Si power HEMTs," *IEEE J. Emerg. Sel. Top. Power Electron.*, vol. 7, no. 2, pp. 679–694, Jun. 2019.

[17] D. Koch, S. Araujo, and I. Kallfass, "Accuracy analysis of calorimetric loss measurement for benchmarking wide bandgap power transistors under soft-switching operation," in *Proc. IEEE Workshop Wide Bandgap Power Devices Appl. Asia*, May 2019, pp. 1–6.

[18] A. Anurag, S. Acharya, and S. Bhattacharya, "An accurate calorimetric loss measurement method for SiC MOSFETs," *IEEE J. Emerg. Sel. Top. Power Electron.*, vol. 8, no. 2, pp. 1644–1656, Jun. 2020.

[19] L. Keuck, N. Jabbar, F. Schafmeister, and J. Boeker, "Switching loss characterization of wide band-gap devices by an indirect identification methodology," in *Proc. Eur. Conf. Power Electron. App.*, Sep. 2018, pp. 1–10.

[20] Z. Zhang, B. Guo, F. F. Wang, E. A. Jones, L. M. Tolbert, and B. J. Blalock, "Methodology for wide band-gap device dynamic characterization," *IEEE Trans. Power Electron.*, vol. 32, no. 12, pp. 9307–9318, Dec. 2017.

[21] W. Wentao, Y. Peng, Y. Kuojun, G. Jian, H. Wuhuang, and Y. Liyue, "De-noising algorithm for digital oscilloscope based on wavelet packet," in *Proc. IEEE Int. Conf. Electron. Meas. Inst.*, Oct. 2017, pp. 233–238.

[22] S. Yin *et al.*, "Automatic V-I alignment for switching characterization of wide band gap power devices," in *Proc. Workshop Wide Bandgap Power Devices Appl. Asia*, May 2018, pp. 75–78.

[23] Tektronix, *Power Meas. Deskew & Calibration Fixture Instructions*, 2008. [Online]. Available: https://www.tek.com/current-probe-manual/067-1686-00

[24] Z. Chen, "Characterization and modeling of high-switching-speed behavior of SiC active devices," Master's thesis, Center Power Electronics Syst., Virginia Polytech. Instit. State Univ., Blacksburg, VA, USA, Dec. 2009.

[25] E. A. Jones *et al.*, "Characterization of an enhancement-mode 650-V GaN HFET," in *Proc. IEEE Energy Convers. Cong. Expo.*, Sep. 2015, pp. 400–407.

[26] B. Callanan, *SiC MOSFET Double Pulse Fixture*, Cree Inc., Durham, NC, USA, 2011.

[27] Z. Zhang *et al.*, "Impact of ringing on switching losses of wide band-gap devices in a phase-leg configuration," in *Proc. IEEE Appl. Power Electron. Conf. Expo.*, Mar. 2014, pp. 2542–2549.

[28] R. Hou, J. Lu, and D. Chen, "Parasitic capacitance Eqoss loss mechanism, calculation, and measurement in hard-switching for GaN HEMTs," in *Proc. IEEE Appl. Power Electron. Conf. Expo.*, Mar. 2018, pp. 919–924.

[29] W. Meng, F. Zhang, G. Dong, J. Wu, and L. Li, "Research on losses of PCB parasitic capacitance for GaN-based full bridge converters," *IEEE Trans. Power Electron.*, pp. 4287–4299, Apr. 2021.

[30] X. Long, W. Liang, Z. Jun, and G. Chen, "A normalized quantitative method for GaN HEMT turn-on overvoltage modeling and suppressing," *IEEE Trans. Ind. Electron.*, vol. 66, no. 4, pp. 2766–2775, Apr. 2019.

[31] R. Hou, J. Xu, and D. Chen, "A multivariable turn-on/turn-off switching loss scaling approach for high-voltage GaN HEMTs in a hard-switching half-bridge configuration," in *Proc. IEEE Workshop Wide Bandgap Power Devices Appl.*, Oct. 2017, pp. 171–176.

[32] Y. Zhang, C. Chen, T. Liu, K. Xu, Y. Kang, and H. Peng, "A high efficiency model-based adaptive dead-time control method for GaN HEMTs considering nonlinear junction capacitors in triangular current mode operation," *IEEE J. Emerg. Sel. Top. Power Electron.*, vol. 8, no. 1, pp. 124–140, Mar. 2020.
[33] EPC, "LTSPICE model of GaN HEMT EPC2014 from EPC." [Online]. Available: https://epc-co.com/epc/Products/eGaNFETsandICs/EPC2014.aspx
[34] EPC, "EPC2014 enhancement mode power transistor." 2013. [Online]. Available: https://epc-co.com/epc/Portals/0/epc/documents/datasheets/EPC2014_datasheet.pdf
[35] W. Lee and B. Sarlioglu, "Design and analysis of integrated planar inductor for GaN HEMT-based zero-voltage switching synchronous buck converter," in *Proc. IEEE Power Energy Conf. Illinois*, Feb. 2018, pp. 1–6.
[36] S. Pan and J. Fan, "Characterization of via structures in multilayer printed circuit boards with an equivalent transmission-line model," *IEEE Trans. Electromagn. Compat.*, vol. 54, no. 5, pp. 1077–1086, Oct. 2012.
[37] D. Reusch and J. Strydom, "Understanding the effect of PCB layout on circuit performance in a high-frequency gallium-nitride-based point of load converter," *IEEE Trans. Power Electron.*, vol. 29, no. 4, pp. 2008–2015, Apr. 2014.
[38] Z. Zeng, J. Wang, L. Wang, Y. Yu, and K. Ou, "Inaccurate switching loss measurement of SiC MOSFET caused by probes: Modelization, characterization, and validation," *IEEE Trans. Instrum. Meas.*, vol. 70, pp. 1–14, 2021.
[39] K. Li, A. Videt, and N. Idir, "GaN HEMT fast switching current measurement method based on current surface probe," in *Proc. Eur. Conf. Power Electron. Appl.*, Aug. 2014, pp. 1–10.
[40] K. Wang, X. Yang, H. Li, L. Wang, and P. Jain, "A high-bandwidth integrated current measurement for detecting switching current of fast GaN devices," *IEEE Trans. Power Electron.*, vol. 33, no. 7, pp. 6199–6210, Jul. 2018.

Minghai Dong (Student Member, IEEE) received the B.Eng. degree in electrical engineering from the Dalian Jiao Tong University, Dalian, China, in 2016. He is currently working toward the Ph.D. degree in electrical engineering with the University of Electronic Science and Technology of China, Chengdu, China.

From November 2018 to May 2019, he was a Research Associate with the SMRT-NTU Smart Urban Rail Corporate Laboratory, Nanyang Technological University, Singapore. His research interests include wide bandgap power-device applications and high power density resonant converters.

Hui Li (Senior Member, IEEE) received the B.S., M.S., and Ph.D. degrees from the Northwestern Polytechnical University, Xi'an, China, in 1983, 1987, and 1991, respectively.

From January 2009 to June 2009, he was a Visiting Scholar with the University of Toronto, Toronto, ON, Canada. He is currently a Professor with the University of Electronic Science and Technology of China, Chengdu, China, where he is also the Dean of the School of Aeronautics and Astronautics. His research interests include the spacecraft simulation and fault diagnosis, space-launching technology, intelligent mechanical electrical systems, and power electronics.

Dr. Li is also a Member of System Simulation Committee of the Chinese Society of Automation, a Member of Chinese Society of Astronautics, and the Director of Chengdu Mechanical Engineering Society.

Shan Yin (Member, IEEE) received the B.Eng. degree in microelectronics from the University of Electronic Science and Technology of China (UESTC), Chengdu, China, in 2010, and the Ph.D. degree in electrical engineering from the Nanyang Technological University (NTU), Singapore, in 2016.

From 2013 to 2016, he was a Research Student and then a Research Fellow with the Rolls-Royce@NTU Corporate Laboratory, NTU, which is a Research Faculty of Rolls-Royce. He is currently an Associate Professor with the China Academy of Engineering Physics, Chengdu. He is also an Adjunct Associate Professor with UESTC. His research interests include wide bandgap power-device applications, gate drivers, high power density converters, power integration, and resonant topologies.

Yingzhe Wu (Member, IEEE) received the B.S., M.S., and Ph.D. degrees in electrical engineering from the University of Electronic Science and Technology of China (UESTC), Chengdu, China, in 2008, 2012, and 2020, respectively.

He is currently a Postdoctoral Research Fellow with the School of Aeronautics and Astronautics, UESTC. His research interests include power electronics, power switching devices, power converter design, and motor driving system.

Dr. Wu was a Reviewer for the IEEE JOURNAL OF EMERGING AND SELECTED TOP. IN POWER ELECTRONICS, the *IET Electrical Power Applications*, and the *IET Power Electronics*.

Kye Yak See (Senior Member, IEEE) received the B.Eng. (first class hons.) degree from the National University of Singapore, Singapore, in 1986, and the Ph.D. degree from the Imperial College London, London, U.K., in 1997.

Between 1986 and 1991, he was with Singapore Technologies Electronics, Singapore, as a Senior Engineer. From 1991 to 1994, he held the position of Lead Design Engineer with ASTEC Custom Power, Singapore. He joined Nanyang Technological University (NTU), Singapore, in 1997, as a Faculty Member. He is currently an Associate Professor with the School of Electrical and Electronic Engineering, NTU. He also holds concurrent appointments as the Director of SMRT-NTU Smart Urban Rail Corporate Laboratory and Electromagnetic Effects Research Laboratory. His research interests include power and signal integrity, electromagnetic compatibility, and real-time condition monitoring of electrical infrastructure.

Dr. See was the Founding Chairs of the IEEE Singapore EMC Chapter and IEEE Singapore Aerospace and Electronic Systems/Geoscience and Remoting Sensing Joint Chapter. He was the Organizing Committee Chairs for 2006 EMC Zurich Symposium and 2008 Asia Pacific EMC Conference; and the General Chairs for 2011 International Symposium of Integrated Circuits, 2015 Asia Pacific Synthetic Aperture Radar Conference, and 2018 IEEE International Conference on Intelligent Rail Transportation. He has been the Associate Editor for the *IEEE Electromagnetic Compatibility Magazine* since January 2012.